Meas. Sci. Technol. **22** (2011) 065902 (7pp) doi:10.1088/0957-0233/22/6/065902

A software simulator for the SPICA Safari instrument

D A Naylor, D J Hayton, J V Lindner and B Sadeghi

Department of Physics and Astronomy, University of Lethbridge, 4401 University Drive, Lethbridge, AB T1K 3M4, Canada

E-mail: naylor@uLeth.ca

Received 1 November 2010, in final form 3 April 2011
Published 4 May 2011
Online at stacks.iop.org/MST/22/065902

Abstract
A software simulator that has been developed for the Safari instrument proposed for the SPace Infrared telescope for Cosmology and Astrophysics (SPICA) mission is presented. The simulator can ingest a range of realistic input spectra and, following a thorough radiative transfer analysis, calculates the power reaching the detector as a function of the optical path difference within the interferometer. The simulator is modular in design so that it can be easily modified to ingest test data as they become available. The simulator will not only find use during the design phase of the Safari instrument, but also during ground performance verification campaigns of the flight model. Through validation of the simulator on ground test data, it will be possible to predict accurately the in-orbit performance of the Safari instrument.

Keywords: imaging Fourier transform spectroscopy, simulator, instrumentation, transition edge superconducting bolometer, SAFARI, SPICA

(Some figures in this article are in colour only in the electronic version)

1. Introduction—SPICA/Safari

The SPace Infrared telescope for Cosmology and Astrophysics (SPICA) mission is a joint JAXA–ESA space astronomy mission optimized for observations at mid- and far-infrared wavelengths. SPICA, with its actively cooled, 3 m class telescope, will provide high spatial resolution observations at unprecedented sensitivity. Since the mid- and far-infrared regions contain a unique suite of diagnostic lines with which to probe the physical and chemical conditions in different regimes, SPICA will address a number of key problems in modern astrophysics, ranging from the star-formation history of the Universe to the formation of planets [1]. One of the focal plane instruments proposed for SPICA is a far-infrared spectrometer (Safari). Safari is being developed by a European/Canadian consortium and features an imaging Mach–Zehnder Fourier transform spectrometer (FTS) of similar design to that of the Herschel/SPIRE instrument [2]. The advantages of FTS are well known: high throughput, simultaneous measurement of all wavelengths, broad spectral coverage, intrinsic wavelength calibration and the best instrumental line shape of any spectrometer [3]. These attributes are particularly desirable in the energy-starved far-infrared spectral region. Building on the space heritage of SPIRE instrument, Safari will provide high-speed mapping spectroscopy, a photometric imaging mode and the flexibility to tailor the spectral resolution to a specific science program [4].

In this paper we describe a software simulator that we have developed for the Safari instrument. The simulator can ingest a range of realistic input spectra and, following a thorough radiative transfer analysis, calculates the power reaching the detector, resulting in the interferogram (the signal produced by a Fourier transform spectrometer). The simulator is modular in design so that it can be readily modified to ingest test data as they become available. The simulator will not only find use during the design phase of Safari but also during ground performance verification campaigns of the flight model. Through validation of the simulator on ground test data, it will be possible to reliably predict the in-orbit performance of Safari.

2. Simulator architecture

The Safari instrument simulator is based on its precursor SHIFTS, the simulator for the Herschel imaging Fourier

transform spectrometer (SPIRE) developed by our group [5], which has been successfully used to predict the performance of the SPIRE instrument [6]. The Safari simulator has been designed to be modular in nature and all modules are referenced to the same time and spectral grids. The software development is implemented in the Interactive Data Language (IDL®), which is well suited for the array manipulation and visualization techniques required in the simulator. The architecture consists of a series of independent and self-contained modules which simulate a physical quantity within the instrument, typically output as a time-series or spectrum. By employing a well-defined set of input and output parameters for each module, this structuring ensures that a new module can be easily integrated without affecting the rest of the simulator. Subsequent changes to an existing module can also be implemented with ease.

The modular component design and the data flow scheme of the simulator are summarized in figure 1. The modular components include the following: *Source Spectral Cube*, *Pointing*, *Spectrometer* (*FTS*), *Optics*, *Power-on-Pixel* and *Detector*. The *optics* module constitutes the core of the simulator, comprised of the telescope and instrument optical components (30+ elements cooled to $\leqslant$6 K) which are divided into three sections (pre-*FTS*, *FTS*, post-*FTS*) and are used to determine the radiant load on the detectors. The *Pointing* module includes contributions from the telescope and the beam steering mirror (BSM). The *Spectrometer* module (spectrometer mechanism) simulates the non-uniform spatial sampling of the interferogram (the signal produced by the interferometer), which is the result of small deviations from uniform velocity that arise in any mechanical translation stage. The total power received at the detectors is computed in the *Power-on-Pixel* module. The only sources which can give rise to a modulated component in the interferogram signal are the astronomical source and any emission from pre-*FTS* optics. Several *Detector* modules were developed to facilitate the simulation and testing of different detector technologies during the design phase of the Safari instrument (e.g. transition edge sensors (TES), silicon bolometers, kinetic induction detectors, photoconductors). Following a detector selection review in 2009, TES detectors were adopted for the Safari instrument [7].

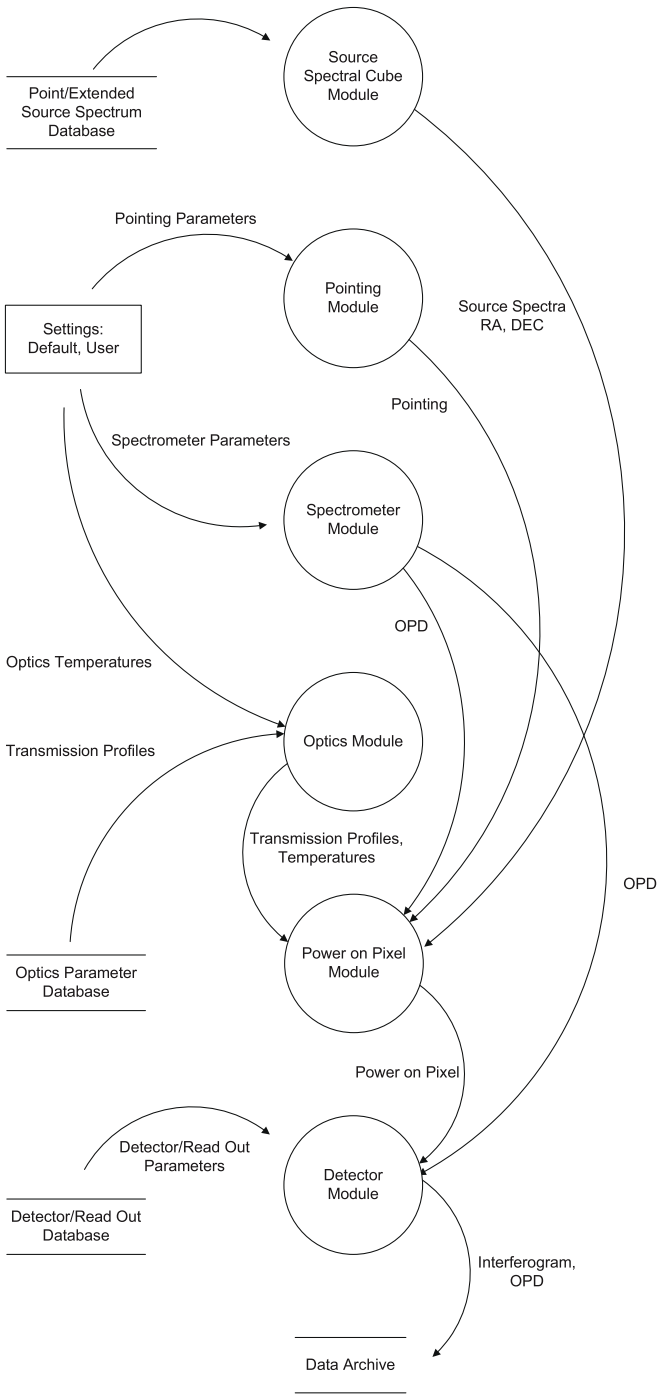

Figure 1. Modular design and data flow diagram for the Safari instrument.

3. *Source Spectral Cube* module

The *Source Spectral Cube* module generates a simulated, time-independent, three-dimensional data cube, with one spectral and two spatial coordinates, expressing spectral intensities in units of W $(\mathrm{cm}^{-1})^{-1}$ m^{-2} sr^{-1}. Point and extended sources are simulated with discrete spectral lines, continua, and combinations of both. The resolution of these simulated input spectra can be chosen to exceed that of the Safari instrument (defined by the maximum optical path difference (OPD) within the interferometer). This will allow one to explore the ability of advanced line fitting techniques to retrieve spectral information beyond the limit of the FTS resolution. In principle, empirical spectra obtained from other space-borne observatories, such as Herschel, could also be ingested into the simulator to bring even greater realism.

4. *Pointing* module

The *Pointing* module consists of two components: pointing of the telescope as a whole (i.e. low-frequency oscillations) and the smaller higher frequency adjustments to the pointing provided by the BSM. Since the Herschel Space Observatory (launched in May 2009) shares many features in common with SPICA, we are planning to use pointing information obtained from Herschel where possible.

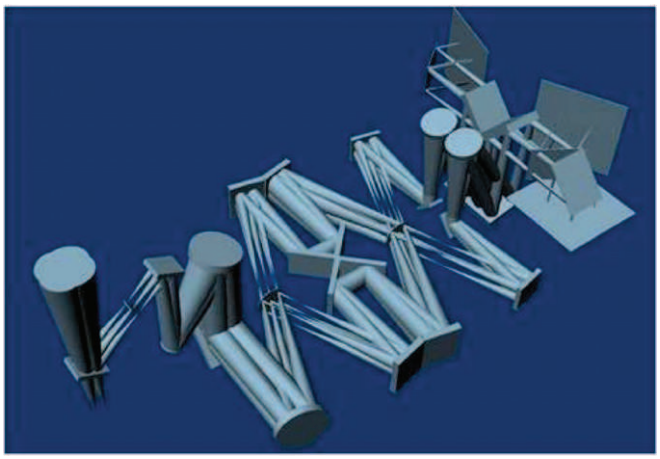

Figure 2. Schematic of one possible optical configuration of the Safari instrument [8].

5. *Optics* module

The simulated optical configuration consists of both a series of elements common to all SPICA instruments and a set belonging specifically to Safari; over 30 components in all (see figure 2). The SPICA primary and secondary mirrors will be actively cooled to a temperature of ∼6 K, while the intermediate components will be cooled to ∼5 K and the detector-box elements to sub-kelvin temperatures [4]. The simulator has been used to study the effects of variations in the temperature of the primary mirror, for each of the three Safari bands. The results are shown in figure 3 which clearly illustrates the steep dependence of flux on telescope temperature in the three Safari bands.

A specific FTS configuration is established by a procedure within the *Optics* module that defines the pre-*FTS*, *FTS* and post-*FTS* optics. The simulator is thus able to accommodate a variety of FTS designs. The sequence of the components is defined by a table containing a temperature time-line and a transmission, emissivity and phase spectral profile for each element. Given a sequential optics table, the *Optics* module computes complex amplitude 'stack' transmission coefficient profiles for all components, divided into pre-*FTS*, *FTS* and post-*FTS* portions. The pre-*FTS* stack transmission amplitude is given by

$$T_{n_{\text{pre-FTS}}}(\sigma) = \prod_{m=n+1}^{N_{\text{pre}}} t_m(\sigma)\, \mathrm{e}^{\mathrm{i}\phi_m(\sigma)}, \qquad (1)$$

where σ is the frequency expressed in wavenumbers, t_m and ϕ_m are the transmission and phase spectral profiles of the mth component of the pre-*FTS* optics, respectively, and N_{pre} is the final pre-*FTS* component. The *FTS* and post-*FTS* stack profiles are computed in a similar fashion. The stack profiles determine what portion of an element's blackbody self-emission contributes to the radiant load on to the detectors at any given time. It is important to note that in an FTS, any emission from pre-FTS optics, including that from the first beam splitter (BS) in the Mach–Zehnder design, results in modulated power as a function of OPD being received at the detectors. Currently the simulator uses theoretical values for the terms in the optics table. As individual sub-system components are manufactured and tested, their measured properties will be used.

6. *Spectrometer* module

In the standard Mach–Zehnder configuration, a single translation stage simultaneously changes the optical paths of the two beams within the interferometer. In one proposed configuration for the Safari instrument, the arms of the classic MZ interferometer are folded, thus reducing the mass and volume of the device, important considerations in space flight applications. Radiation from the astronomical source beam is divided into two beams by the first BS. The reflected and transmitted beams are directed to complementary mirrors and then onto the moving, back-to-back, roof-top mirrors (where the optical retardation is introduced), before recombining at the second BS and subsequently being focussed onto the detector arrays.

In calculating the OPD between the two interfering beams, the simulator mimics the stage velocity of the scanning mirrors according to the velocity error spectral profile, which will be determined during component testing. By way of illustration, figure 4 shows the impact of velocity jitter on the measured interferogram (upper-left panel) and recovered spectrum (upper right panel) for the shortest wavelength Safari band where the effects of velocity jitter area more pronounced. The velocity error profile used to generate these results was based on data obtained from the SPIRE instrument during pre-flight testing.

It is common practice in Fourier spectroscopy to measure the interferogram in equal intervals of OPD. However, this is not practical for a space-based mission, and as with the Herschel/SPIRE FTS, Safari will measure the detector signal and the stage position at different times. Subsequent analysis will require interpolation onto the same time, and ultimately, OPD grid. At any given time in the universal time grid, the simulator computes both the position and the flux falling on the detector. The resulting time-series are fed to the *Power-on-Pixel* module where the OPD-dependent phase term is introduced.

7. *Power-on-Pixel* module

In order to compute the astronomical power received by a detector within its field of view (FOV), *Power-on-Pixel* first determines the FOV according to the telescope's pointing coordinates. A wavelength-dependent FOV is introduced to account for the effects of diffraction. In this way, *Power-on-Pixel* sums over the spatial coordinates and returns the total power received by a detector within its FOV at a particular wavelength.

As discussed above, the self-emission of all optical components positioned after the pre-*FTS* portion of the design is unmodulated, while the astronomical source and pre-*FTS* optics emission experience modulation due to the varying

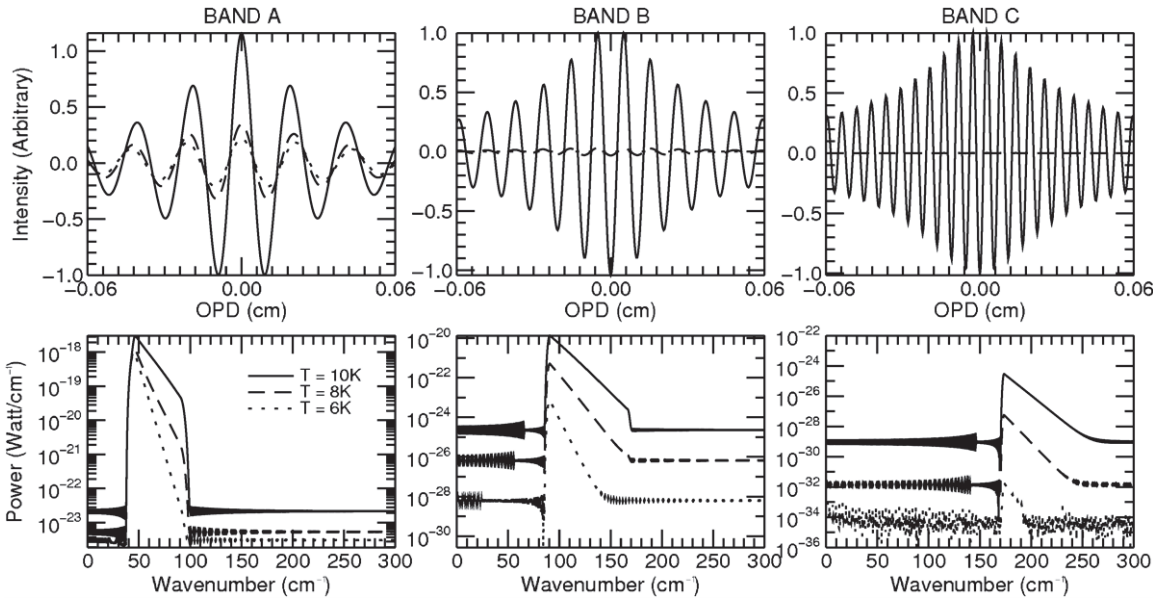

Figure 3. A comparison of primary mirror emission at 6, 8 and 10 K shown in terms of the generated interferograms (*upper plots*) and the corresponding recovered spectra (*lower plots*) for the three nominal bands of the Safari instrument. A frequency-dependent mirror emissivity model has been adapted from the Herschel/SPIRE sensitivity model [9] resulting in a mirror emissivity of between 0.5% and 1%. The inversion of the interferogram signal of band A relative to bands B and C is due to the complementary nature of the two output ports of any interferometer. In this case band A views one output port, while bands B and C both view the complementary output port by use of a dichroic beam splitter.

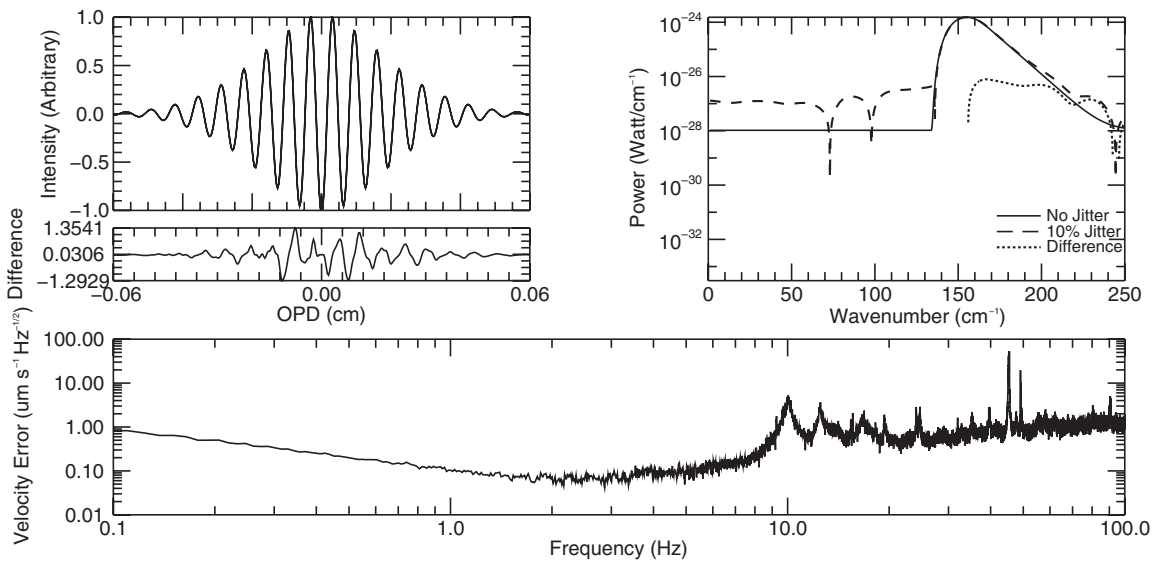

Figure 4. The effect of the mirror velocity jitter at 0% and 10%. Simulated interferograms for the two cases are given in the upper-left-top plot while the difference between the interferograms ($\times 100$) is given in the upper-left-bottom plot. The corresponding recovered spectra are provided in the upper-right plot. The simulator generates a realistic spectral velocity jitter profile based on the spectral profile of velocity error measured from the Herschel SPIRE proto-flight mechanism in 2005.

OPD. The resulting magnitude of the electric field, $\vec{E}$, of the radiation entering the FTS can be expressed as

$$E_{\mathrm{pre}} = \left[\frac{2}{c\epsilon_0} \left(P_{\mathrm{sky}} |T_{1_{\mathrm{pre\text{-}FTS}}}|^2 + \sum_{m=1}^{N_{\mathrm{pre}}} \varepsilon_m B_m |T_{m_{\mathrm{pre}}}|^2 \right) \right]^{\frac{1}{2}}, \quad (2)$$

where the frequency dependence has been omitted for clarity. $P_{\mathrm{sky}}(t, \sigma)$ is the power received from the astronomical source, with $T_{1_{\mathrm{pre\text{-}FTS}}}$ its corresponding transmission up to the entrance of the FTS, ϵ_m is the emissivity and $B_m(t, \sigma)$ is the blackbody emission of the mth optical component, and $T_m(\sigma)$ is the corresponding transmission amplitude. The wavelength-dependent throughput is also taken into account but is omitted for clarity. The phase modulation introduced by the varying OPD is computed at the second BS of the FTS, where the $\vec{E}$-fields of the recombining beams for one of the complementary outputs can be expressed as

$$\begin{aligned} \vec{E}_{\uparrow} &= E_{\mathrm{pre}}(R_{1_i}\, \mathrm{e}^{\mathrm{i}\phi_{r_i}} R_{1_c}\, \mathrm{e}^{\mathrm{i}\phi_{r_c}}\, \mathrm{e}^{\mathrm{i}\sigma z} + T_1\, \mathrm{e}^{\mathrm{i}\phi_t} T_2\, \mathrm{e}^{\mathrm{i}\phi_t}\, \mathrm{e}^{-\mathrm{i}\sigma z}) \\ \vec{E}_{\downarrow} &= E_{\mathrm{pre}}(R_{1_i}\, \mathrm{e}^{\mathrm{i}\phi_{r_i}} T_2\, \mathrm{e}^{\mathrm{i}\phi_t}\, \mathrm{e}^{\mathrm{i}\sigma z} + T_1\, \mathrm{e}^{\mathrm{i}\phi_t} R_{2_i}\, \mathrm{e}^{\mathrm{i}\phi_{r_i}}\, \mathrm{e}^{-\mathrm{i}\sigma z}), \end{aligned} \quad (3)$$

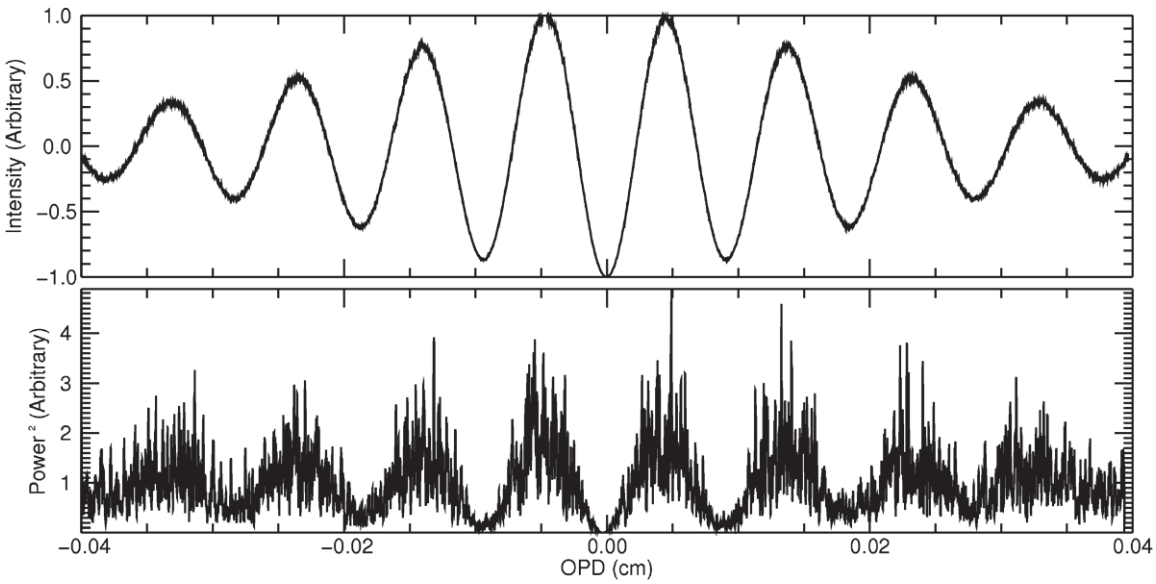

Figure 5. Simulated photon noise for band C viewing a 10 K source. The upper plot shows the interferogram including photon noise. The lower plot shows the variation of the noise, expressed as the square of the difference between the interferogram in the upper plot and the equivalent noise-free interferogram, as a function of OPD. In this representation the noise should approach zero in the dark fringe region, 2 in the bright fringe region and 1 in the wings of the interferogram, as is observed.

where $T_1(\sigma)$ and $T_2(\sigma)$ are the transmission amplitudes of the first and second beam splitters; $R_{1_i}(\sigma)$, $R_{2_i}(\sigma)$, $R_{1_c}(\sigma)$ and $R_{2_c}(\sigma)$ are the reflection amplitudes of the inductive and capacitive sides of each BS with $\phi_{t,r}$ being their corresponding phases, σ is the spectral grid in wavenumbers, and $z(t)$ is the time-dependent OPD.

In the final step, the unmodulated portion of the total power, $P_{\text{post}}(t, \sigma)$, is combined with the modulated component to determine the total power incident on a detector pixel at a given output port and a given time:

$$P_{\text{post}} = \sum_{m=m_{\text{FTS}}}^{N_{\text{post-FTS}}} B_m |T_m|^2$$
$$P_{\uparrow} = \frac{c\epsilon_0}{2}|E_{\uparrow}|^2 + P_{\text{post}} \tag{4}$$
$$P_{\downarrow} = \frac{c\epsilon_0}{2}|E_{\downarrow}|^2 + P_{\text{post}}.$$

Once the total power received by each detector has been determined, the photon noise is calculated from the Poisson statistic of the average number of photons arriving at the detector each second and added to the total power. Figure 5 shows the interferogram obtained when viewing a 10 K source in the short-wavelength band (band C) of Safari and the associated photon noise as a function of OPD. The noise is seen to be small in the regions of destructive interference (corresponding to dark fringes), maximum in the regions of constructive interference (bright fringes) and uniform and equal to the $\sqrt{2}$ of the maximum value at high OPD.

8. *Detector* module

The integration of the power falling on the detector over the spectral range defined by the band-limiting filters is computed in the *Detector* module. First the detector coupling and quantum efficiency are applied to the incident spectral power. The product of the detector spectral responsivity (V W^{-1}) and the incident power is then integrated across the spectral band, resulting in the instantaneous value of the interferogram:

$$V(t) = \int P(t, \sigma) R(\sigma)\, \mathrm{d}\sigma. \tag{5}$$

Initial noise-equivalent-power calculations are performed assuming that the detector will be photon noise-limited (other noise sources such as Johnson, phonon, etc are detector specific and can be added at this stage).

Regardless of the choice of the detector technology, the combination of thermal, temporal and electrical responses must also be taken into account. These are combined into a detector-specific response function, which is convolved with the time-varying power incident on the detector to simulate the response of the detection system to the modulated optical power as the optical path within the interferometer is scanned.

The final step in the *Detector* module is the construction of a synthetic data product defined by the detector voltages and OPD as a function of time. In general, the detector voltages and OPD will be sampled on different time grids due to limitations of on-board electronics and telemetry. The resulting time-series are saved to a file in FITS format.

Since different detector types have unique couplings, spectral responsivities, quantum efficiencies, and frequency response characteristics, a unique detector module is required for each detector to be simulated. The modular nature of the *Detector* module simplifies the evaluation of different detector types and configurations.

Currently, our group is involved with the design and fabrication of voltage-biased superconducting bolometers (VSB) [10]. VSBs operate on a similar principle to that of TES bolometers, the most significant difference being that VSBs are

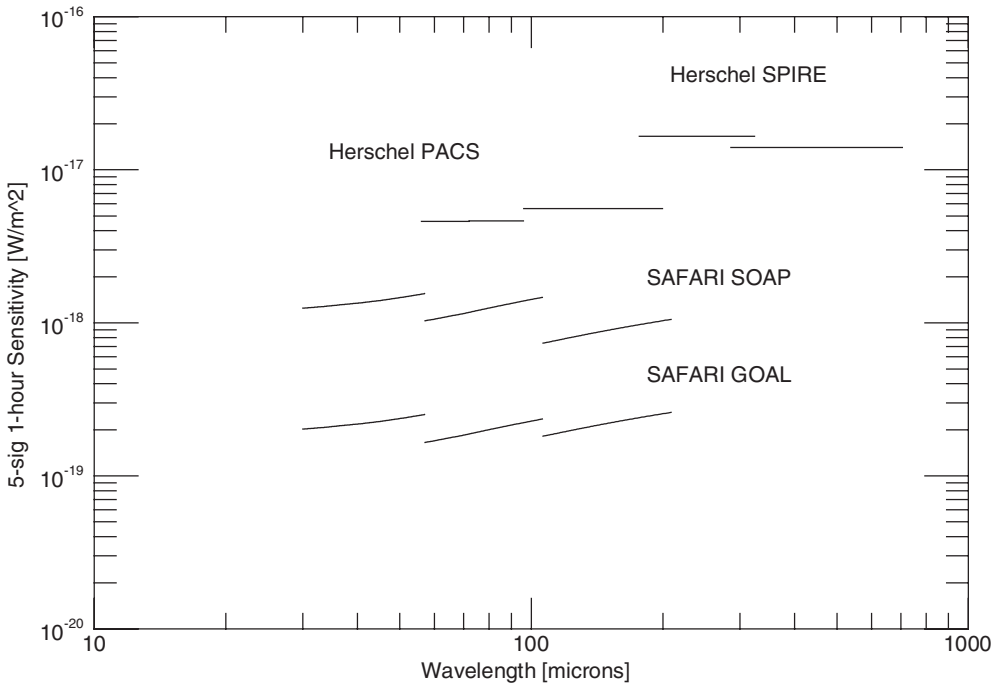

Figure 6. Predicted spectroscopic performance of the Safari instrument.

higher resistance devices and therefore do not require SQUID readouts. The modular nature of the simulator has allowed its use in predicting the performance of a laboratory-operated FTS coupled to a cryogenic VSB detector.

9. Sensitivity calculations

While several detector options were initially considered, the maturity of TES bolometers has lead to their adoption for the Safari instrument. TES devices consist of superconducting thin films that are biased at the midpoint of the normal to superconducting transition, where they are intrinsically linear devices. With a very high temperature coefficient of resistance, they experience large changes in resistance with small changes in temperature, resulting in an extremely sensitive device. A change in incident photon flux results in a change in the current through the TES to maintain the operating point of the detector at the midpoint of the transition. This current represents the measured signal [11].

Figure 6 shows the band coverage and predicted point source sensitivities for spectroscopic observations possible with Safari, determined using the simulator described in this paper. The state-of-the-art detector performance (SOAP) is based on Si:Sb BIB and Ge:Ga photoconductors, and the Goal performance is based on TES bolometers, with the zodiacal background taken as the limiting photon noise source [12]. The zodiacal light places a fundamental limit on what can be achieved from any space-borne far-infrared telescope. Also shown for comparison are the estimated sensitivities of the Herschel/SPIRE and PACS instruments [13, 14]. It can be seen that there exists potentially two orders of magnitude improvement in sensitivity as a direct result of having an actively cooled telescope. The challenge is to develop detectors that can exploit this extremely low background environment.

As an example of the flexibility of the simulator, our group has developed an imaging FTS (FTS-2) for use with the SCUBA-2 TES bolometer array [15] at the James Clerk Maxwell Telescope. This will be the first time that TESs will be used in conjunction with an astronomical imaging FTS, and so it will provide the community with a unique technology demonstrator for Safari. Although observations with FTS-2 are complicated by having to observe through the Earth's atmosphere, the atmosphere can be simulated as an additional pre-*FTS* optical element of the appropriate spectral transmission and emissivity. The flexibility of the simulator is such that it can be easily reconfigured to model the performance of FTS-2, which is due to be commissioned in mid-2011.

10. Summary

We have developed a simulator for the proposed Safari instrument on the SPICA mission. The simulator extends earlier work by Lindner *et al* [16], which was used successfully to model the SPIRE instrument [6]. The Safari simulator improves on the SPIRE simulator by incorporating a wavelength-dependent FOV, self-emission from all optical components, and by allowing the comparison of the performances of different detector and readout technologies.

Since Safari and SPIRE have many features in common, by using empirical SPIRE data we will be able to model more realistically the predicted performance of SPICA. We anticipate that the simulator will find a range of uses throughout the lifetime of the project, from studying trade-offs in the design and interpreting ground test data, to predicting

the in-orbit performance of the instrument. The simulator will also act as a medium for demonstrating the advantages of SPICA over Herschel.

Acknowledgments

This work is funded with support by the Canadian Space Agency (CSA), in support of the missions selected for study by the European Space Agency (ESA) Cosmic Vision Program, and NSERC. The authors acknowledge Coskun Oba for providing some of the simulations presented in this paper.

References

[1] Nakagawa T 2009 SPICA Team *SPICA Workshop Proc.* 01001

[2] Griffin M *et al* 2007 The Herschel-SPIRE instrument and its capabilities for extragalactic astronomy *Adv. Space Res.* **40** 612–9

[3] Davis S P, Abrams M C and Brault J W 2001 *Fourier Transform Spectrometry* (New York: Academic)

[4] Nakagawa T 2008 SPICA mission for mid- and far-infrared astronomy *Proc. SPIE* **7010** 70100H

[5] Lindner J V, Naylor D A and Swinyard B M 2006 SHIFTS: simulator for the Herschel imaging Fourier transform spectrometer *Proc. SPIE* **6265** 62652Y

[6] Spencer L, Naylor D and Swinyard B 2010 Performance evaluation of the Herschel/SPIRE imaging FTS through ground-based measurements *Meas. Sci. Technol.* **21** 065601

[7] SPICA Consortium 2009 SPICA Assessment Study Report *SPICA Int. Consortium Doc.* ESA Document ESA/SRE(2009)6

[8] Swinyard B M *et al* 2008 The European contribution to the SPICA mission *Proc. SPIE* **7010** 70100I

[9] Fischer J, Klassen T, Hovenier N and Jakob G 2004 Cryogenic far-infrared laser absorptivity measurements of the Herschel Space Observatory telescope mirror coatings *Appl. Opt.* **43** 3765

[10] Hayton D J, Naylor D A, Zhang Y, Mauskopf P, Ade P A R, Dunscombe C, Wood K and Cox J 2010 Cryogen-free operation of a voltage-biased superconducting bolometer *Proc. 35th Int. Conf. on Infrared, Millimeter and Terahertz Waves (IRMMW-THz)* doi:10.1109/ICIMW.2010.5612399

[11] Irwin K D and Hilton G C 2005 Transition-edge sensors *Cryogenic Particle Detection (Springer Topics in Applied Physics 99)* (Berlin: Springer) pp 81–97

[12] Griffin M 2007 SAFARI sensitivity model *Cardiff University Technical Report* SPIRE-QMW-NOT-000642

[13] Griffin M *et al* 2010 The Herschel-SPIRE instrument and its in-flight performance *Astron. Astrophys.* **518** L3, 21–7

[14] Poglitsch A *et al* 2010 The photodetector array camera and spectrometer (PACS) on the Herschel Space Observatory *Astron. Astrophys.* **518** L2, 9–20

[15] Naylor D A and Gom B G 2004 SCUBA-2 imaging Fourier transform spectrometer *Proc. SPIE* **5159** 91

[16] Lindner J V 2008 SHIFTS: simulator for the Herschel imaging Fourier transform spectrometer *MSc Thesis* University of Lethbridge, AB, Canada